CAAP Quarterly Report

Date of Report: *January 7, 2015*

Contract Number: *DTPH5615HCAP03*

Prepared for: *James Prothro, PHMSA-DOT*

Project Title: *Bayesian Network Inference and Information Fusion for Accurate Pipe Strength and Toughness Estimation*

Prepared by: *Arizona State University, University of Colorado-Denver*

Contact Information: *Dr. Yongming Liu and Dr. Yiming Deng*

For quarterly period ending: *January 10, 2015*

Business and Activity Section

(a) Generated Commitments

The United States system for natural gas pipelines consists of 210 systems overall running through the different states. A majority of these pipelines have been laid down in the early 1900's, and thus lack reliable information for the aging pipeline systems which marks a concern for pipeline safety and integrity. At the present date, 63 percent these pipelines contain too many twists and turns that do not allow the conventional methods of inspection such as pipeline inspection gauge (PIG), or automatic robots to be used in such situations. Due to these, pipeline infrastructure forms a critical aspect for US economy and therefore accurate pipe strength determination is crucial. Due to the various gaps that exist in terms of uncertainties the accurate strength estimation, a novel approach using multimodality diagnosis and information fusion framework has been proposed, and forms the main objective of the present work. This project is to involve estimation of the basic material properties; microstructure, composition etc. as well as various surface mechanical properties. A different aspect of the project will look into advanced testing methods for property estimation with the use of acoustic and electromagnetic sensors. And the last part would include fusion of the various data and correlations into a multimodal system to integrate these and obtain a probabilistic strength and toughness with a high degree of accuracy. With an evolution of the pipe steel grades from API X40 through API X80 in the present date, a good control over processing parameters have been achieved. However, for the earlier grades, X42, X52 etc. such processing control was not the case, and hence there is a great amount of property and strength variation observed in these steel grades. As these pipeline systems still remain a vital part of the current service pipelines, a reliable source of information is thus required and hence the focus of our work will be on X42 steel grade.

Several major tasks are proposed to address the above-mentioned project objectives/goals. Experimental testing, advanced data analysis, numerical simulation, and probabilistic methods are integrated in the proposed tasks. A summary is listed below and detailed work plan will be discussed in the following sections.

Task 1. Experimental testing and data analysis of chemical, metallurgical, and mechanical properties of pipe steel (Arizona State University) This task focuses on the information obtaining and analysis about the basic pipe steel properties. Both in-house experimental testing and literature data will

be used for this task. First, in situ and ex situ chemical composition analysis will be performed for several representative pipe steel specimens (from online vendors and our industry collaborators). Optical emission spectrography (OES) and energy dispersive spectroscopy (EDS) will be used for in situ and ex situ measurements of chemical composition, respectively. Following this, in situ and ex situ pipe steel microstructure analysis will be performed to obtain the grain structure images using etching-based optical microscopy and electron back scattered diffraction (EBSD) images, respectively. Imaging analysis will be performed to obtain the statistical information and metrics about the pipe steel microstructure, such as grain size distribution. Next, surface hardness measurements will be performed using portable ultrasound hardness testers and the results will be correlated with pipe strength and toughness. Advanced data analysis using Gaussian Process modeling will be used for surrogate modeling and to quantify the uncertainties for future Bayesian network inference.

Task 2. Experimental testing, data analysis and prototyping for acoustic and micro-electromagnetic electromagnetic properties of pipe steel (University of Colorado-Denver) This task focuses on the information obtaining and analysis about the pipe steel acoustic and micro-electromagnetic properties. First, ex situ low-frequency near-field microwave microscopy analysis will be performed for several representative pipe steel specimens. Obstacles for dislocation movement, such as grain boundaries and void inclusions, will be revealed in terms of measurable electromagnetic properties. Following that, surface and subsurface microstructural image analysis assisted by multi-physics modeling will be carried out to understand the correlations between steel strength and different possible mechanisms which impede the dislocation movement under load in the micro-electromagnetic spectrum. Next, a prototype of integrating magnetostriction and pulsed eddy current-based Barkhausen noise imaging system will be developed to characterize the pipe steel's Bloch wall jumps and the results will be correlated with pipe strength and toughness experimentally with advanced data analysis.

Task 3. Bayesian network for information fusion and probabilistic pipe strength estimation (Arizona State University and University of Colorado-Denver). This task will focus on the development of a novel Bayesian network for the inference of pipe strength. First, the network structure and conditional probability estimation will be performed using the multi-modality diagnosis data obtained in Tasks 1&2. Following this, parametric studies with synthetic data using the developed Bayesian network will be performed to investigate the behavior and performance of the information fusion framework. Sensitivity analysis will be performed to identify the important factors in the proposed Bayesian network. Finally, model verification and validation with realistic field/laboratory measurements will be demonstrated. Probabilistic pipe strength estimation and associated risk-based confidence determination will be quantified.

A schematic illustration of the proposed components and their integration is shown in Fig. 1. The philosophy behind the proposed methodology is that each modality diagnosis will contain part of the information about the pipe steel strength and a fusion process will, in principle, provide more accurate estimation of the current state of the aging pipes. This schematic illustration also indicates the multidisciplinary collaborative work of the proposed study. Mechanical and material research (ASU), electrical and acoustic study (CU-Denver), and industrial experiences about the manufacturing and operation (GTI) are integrated together for the probabilistic pipe strength estimation and future decision making for risk mitigation.

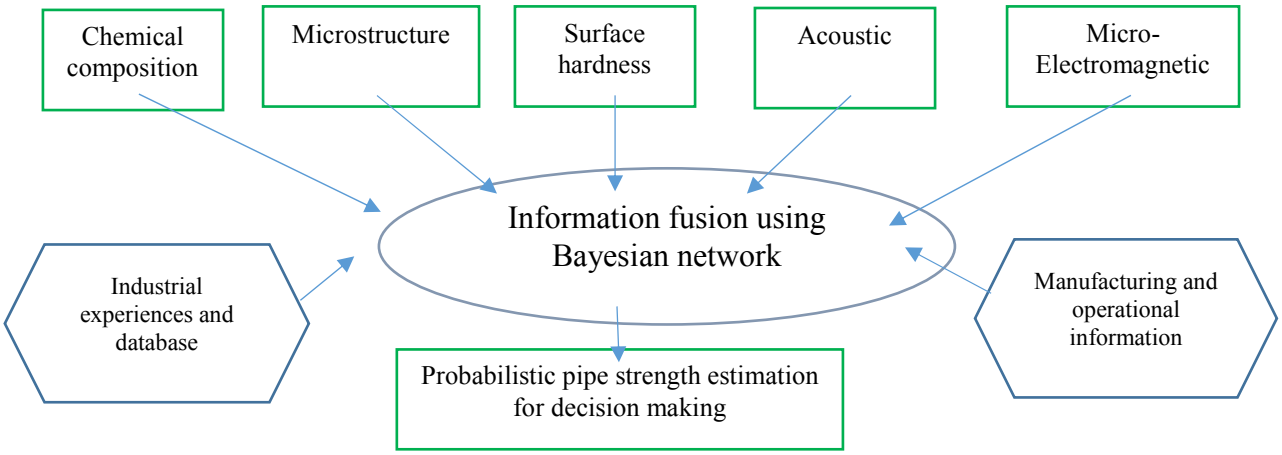

Fig. 1 Schematic illustration of the proposed pipe strength estimation framework

(b) Status Update of Past Quarter Activities

Task 1. Experimental testing and data analysis of chemical, metallurgical, and mechanical properties of pipe steel

SUMMARY

In a view of the above description, several literature studies have been carried out to obtain a good understanding of the present situation. The first step of the study will deal with a thorough literature review to investigate the chemical and mechanical properties, such as composition, microstructure, stress-strain behavior, processing conditions etc. widely available in the modern literature, thus eliminating the need to perform in-situ tests and allowing us to concentrate more vital aspects of the work. The second aspect involves study was to establish correlations between the different microstructural and chemical parameters and steel strength to be used as an input to Bayesian network fusion model. The third part deals with development of methods for in-situ investigation of the mechanical properties through the design of an ABI fixture. The information from this part will be input into the strength correlation equations and be integrated to finally form a network fusion model. In addition to this, we are in the process of obtaining the representative pipeline samples from GTI in order to conduct testing for property variation along the pipe wall thickness and collect data for input into the model.

CONTENT:

Section I:

Mechanical properties of API 5X steel grades

- Description of API 5X grades and their general mechanical properties
- Chemical composition of the different grades.
- Stress-strain curves for the API X42 grade from two different pipeline companies.

Section II:

Correlation of the different material parameters to steel strength

- Relationship of volume fraction of constituent phases to stress-strain behavior
- Microstructure correlation to yield ratio
- Strength correlation to the different phases of steel
- Strength correlation to hardness of steel

- Hardness correlation to Carbon equivalent

Section III:
References and Future Work
Section IV:
Design of the ins-situ ABI fixture

SECTION I:
API 5L STEEL GRADES AND THEIR PROPERTIES

The API 5L stands for the American Petroleum Institute specification and covers seamless and welded steel line pipe suitable for use in conveying gas, water, oil, and other liquefied media. The different grades use the designation X followed by the specified minimum yield strength of the pipe steel. The following are the mechanical and chemical properties of the different steel grades [1]:

1. Mechanical Properties

API 5L Grade	Yield Strength min. (ksi)	Tensile Strength min. (ksi)	Yield to Tensile Ratio (max.)	Elongation min. %[1]
A	30	48	0.93	28
B	35	60	0.93	23
X42	42	60	0.93	23
X46	46	63	0.93	22
X52	52	66	0.93	21
X56	56	71	0.93	19
X60	60	75	0.93	19
X65	65	77	0.93	18
X70	70	82	0.93	17
X80	80	90	0.93	16

2. Chemical Composition

PSL-1	Carbon	Maganese	Phosphorus	Sulphur	V	Nb	Titanium
Grade A	0.22	0.90	0.03	0.03	-	-	-
Grade B	0.26	1.20	0.03	0.03	c,d	c,d	d
Grade x 42	0.26	1.30	0.03	0.03	d	d	d
Grade x 46	0.26	1.40	0.03	0.03	d	d	d
Grade x 52	0.26	1.40	0.03	0.03	d	d	d
Grade x 56	0.26	1.40	0.03	0.03	d	d	d
Grade x 60	0.26	1.40	0.03	0.03	f	f	f

c = (Nb+V)≤ 0.06 %
d = (Nb+V+Ti)≤ 0.15 %
f = Unless otherwise agreed (Nb+V+Ti)≤ 0.15 %

PSL-2	C	Mn	P	S	Si	V	Nb	Ti
Grade B	0.22	1.20	0.025	0.015	0.450	0.050	0.050	0.04
Grade x 42	0.22	1.30	0.025	0.015	0.450	0.050	0.050	0.04
Grade x 46	0.22	1.30	0.025	0.015	0.450	0.050	0.050	0.04
Grade x 52	0.22	1.40	0.025	0.015	0.450	d	d	d
Grade x 56	0.22	1.40	0.025	0.015	0.450	d	d	d
Grade x 60	0.12	1.60	0.025	0.015	0.450	g	g	g

c = (Nb+V)≤ 0.06 %
d = (Nb+V+Ti)≤ 0.15 %
g = Unless otherwise agreed (Nb+V+Ti)≤ 0.15 %

Where,

PSL 1 is a standard quality for line pipe whereas PSL 2 contains additional chemical, mechanical properties, and testing requirements.
PSL-1; Weld seam of each pipe shall be tested by online Eddy current test , PSL-2; Steel skelp and wald seam shall be tested by Ultrasonic test

API 5L X42

Measurement of properties through ABI and miniature tensile tests conducted at the facilities of Advanced Technology Corporation (ATC). Miniature tensile test specimens were prepared from different pipe materials with their axes in the circumferential direction. Further, comparisons of the yield strength values and the stress-strain curves from the ABI and the miniature tensile tests have been show to demonstrate an excellent correlation [2].

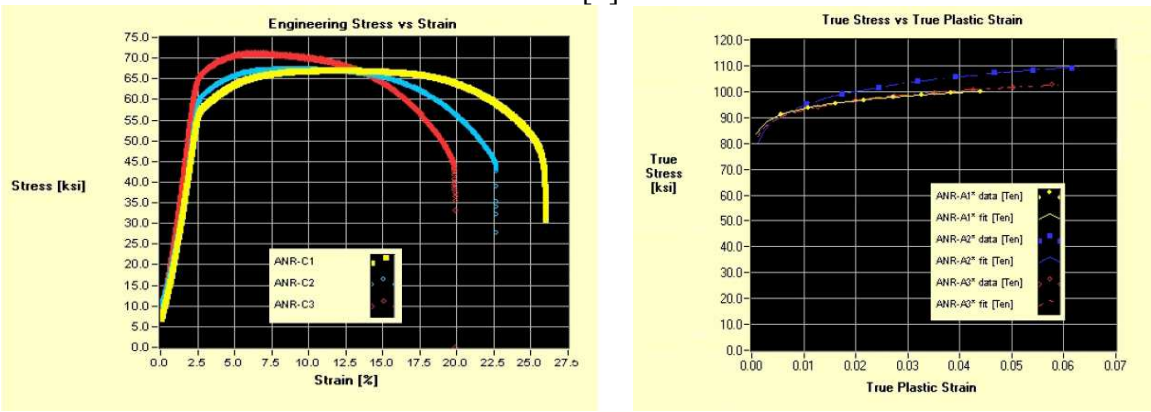

Fig: Engineering and True Stress-Strain Curves from three miniature tensile specimens of X42 pipelinesteel from ANR Pipeline Company[2].

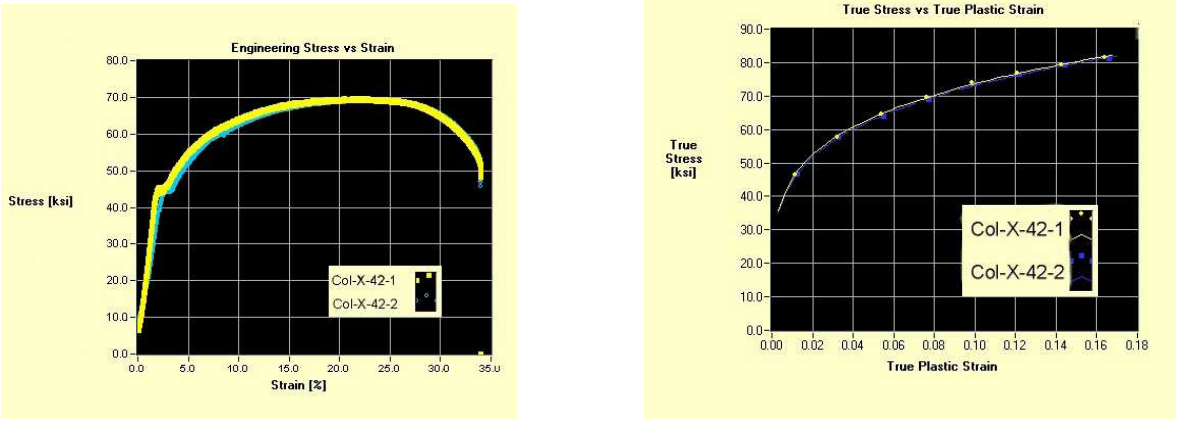

Fig: Engineering and True Stress-Strain Curves from two miniature tensile specimens of X42 pipeline Steel from Columbia Gas[2]

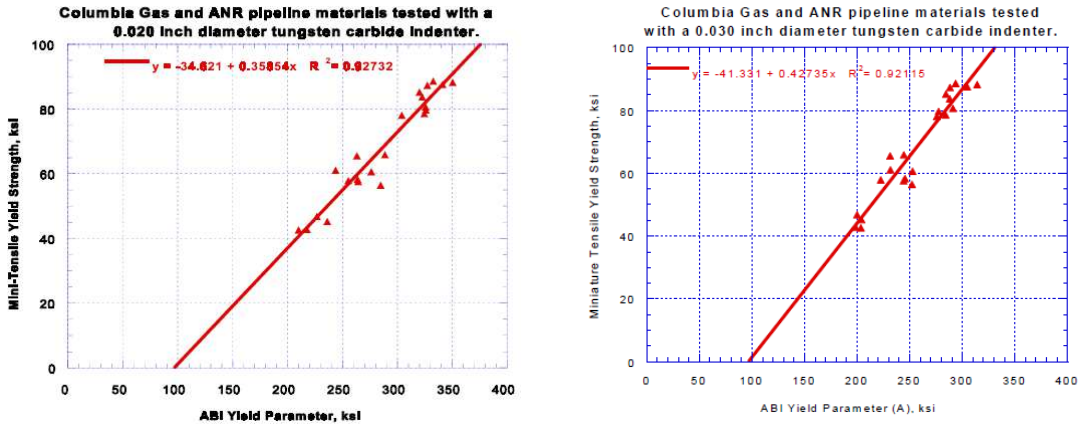

Fig: Correlation between the ABI yield parameter and the yield strength using a 0.020-inch and 0.030-inch diameter tungsten carbide indenter from miniature tensile tests of seven pipeline specimens [2]

SECTION II:

MICROSTRUCTURAL CORRELATION TO MECHNAICAL PROPERTIES OF STEEL

1. Relationship of volume fraction of constituent phases to stress-strain behavior

The reference literature used a micromechanics approach to predict the stress strain relationship of a DP steels (Ferrite-bainite/ Ferrite-pearlite). The model is based on considerations of Eshelby's inclusion theory, the Mori-Tanakameanfield concept and the von Mises type plastic flow rule. As per this study, the stress-strain curve could be divided into three stages and each of them could be linked to the volume fraction of the constituent phases and hence a means to control the stress-strain relationships and the resulting work hardening behavior could be obtained.

Microscopic examinations were conducted to investigate the chemistries of the constituent phases in addition to the thermodynamic data. For the purpose of investigation of volume fractions of the different phases in the steels, the process involved a metallographic sample prep and SEM analysis. The areas of each of the constituent phases were graphically marked and measured which was then regarded as representative for the volume fraction of the each phase in the examined DP-steel.

SEM Micrographs of the two investigated steels reveal the different structures. The white portion refers to Ferrite in both the images and the dark region corresponds to martensite/bainite.

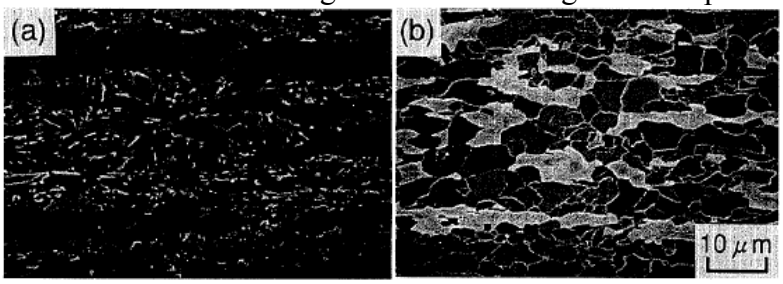

Fig: SEM Micrographs: a) Ferrite and martensite b) Ferite and bainite [3]

Chemical composition of the DP steel(mass%)

C	Si	Mn	Nb	V
0.08	0.3	1.5	0.05	0.05

Further, the chemical composition of each of the constituent phases was calculated with the use of average carbon content and the calculated volume fractions.

	C	Si	Mn	Nb	V
Ferrite	0.015	0.3	1.5	0.05	0.05
Martensite	0.6	0.3	1.5	0.05	0.05
Bainite	0.2	0.3	1.5	0.05	0.05

This different carbon content of the constituent phases are likely to impart the different levels of strength to them, and therefore, a difference in the volume fraction of these for the different steel, causes a great effect on the stress strain behavior.

The stress strain behavior of the steels was then investigated, which led to a set of hardening indexes and the corresponding impact on the flow curve as per the relation;

Ferrite: $\sigma = 675 \cdot (0.002 + \varepsilon_p)^{0.0568}$ [MPa]

Martensite: $\sigma = 3\,560 \cdot (0.0001 + \varepsilon_p)^{0.21}$ [MPa]

Bainite: $\sigma = 1\,470 \cdot (0.0005 + \varepsilon_p)^{0.142}$ [MPa]

Pearlite: $\sigma = 1\,298 \cdot (0.002 + \varepsilon_p)^{0.108}$ [MPa]

Steel	Carbon content, %	Volume fraction	Hardening index	
			Stage II	Stage III
Ferrite-Martensite	0.6	0.12	0.13	0.12
Ferrite-Bainite	0.2	0.33	0.29	0.12
Ferrite-Pearlite	0.7	0.07	0.12	0.07

Some of the results showing the impact of these volume fractions are as follows:

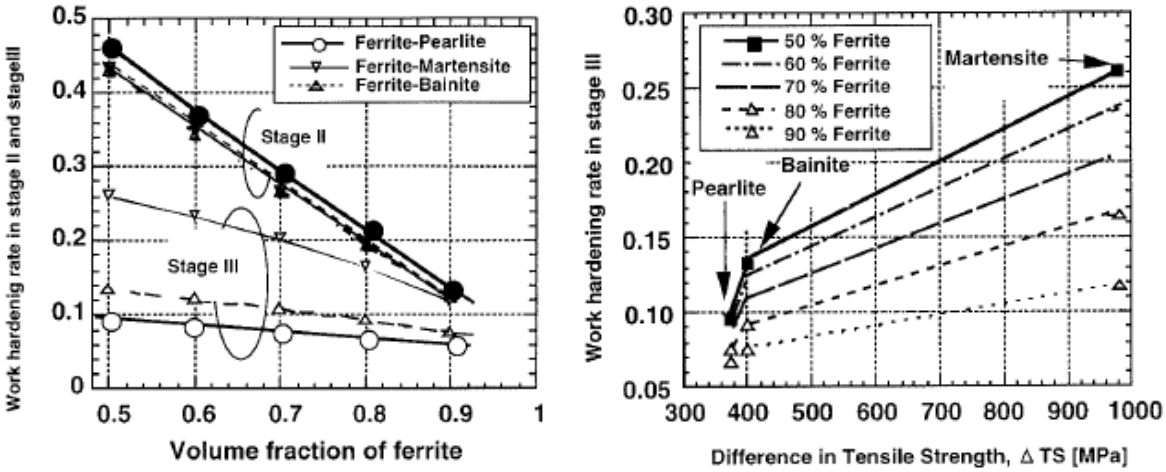

Fig: Impact of volume fraction on the work hardening behavior [3]

It can be followed that with the decrease in the ferrite volume fraction, the hardening index increases considerably [3].

2. Relationship of Microstructure to the Yield Ratio

In the present study, a number of alloy systems have been investigated eg: Ferrite, Ferrite-pearlite steels etc. to the effects of microstructural features on the yield ratio(yield strength/tensile strength) of high strength linepipe steels. In general, the pipe steels require a lower yield ratio which allows higher resistance to deformation from yielding to plastic instability. Different combinations of chemical composition and processing conditions were used to design the different kinds of steel [Ref]. These were followed by tensile and charpy tests at a range of temperatures. The fracture surfaces were characterized using SEM, whereas, the volume fraction and grain size of the constituent phases were analyzed with an image analyzer.

The following figure shows the different microstructures for the different steels:

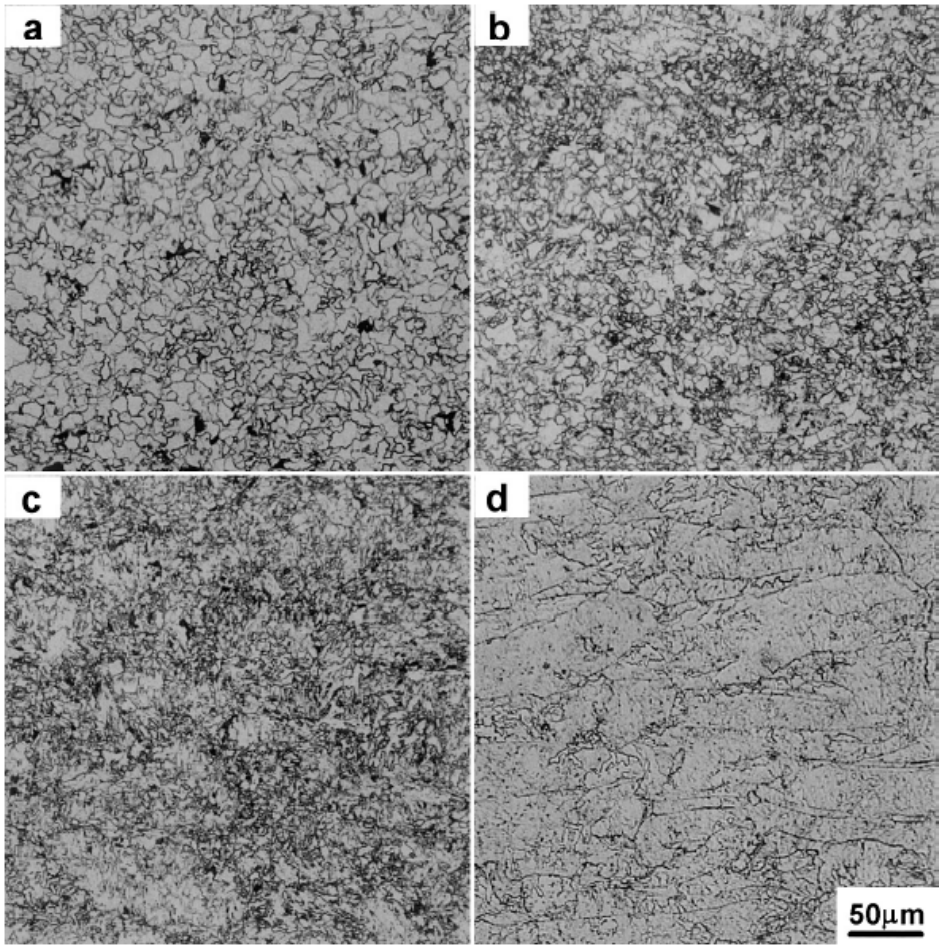

Fig: Microstructures: (a) ferrite–pearlite steel (B steel), (b) ferrite steel with acicular ferrite as second phase (C steel), (c) acicular ferrite steel with polygonal ferrite as second phase (D steel), and (d) bainite steel (G2 steel) [4].

Table1: Quantification of grain size and volume fraction of the phases [4]

Structure	Steel	Ferrite Grain Size (μm)	Vol. % of Second Phase		
			Ferrite (%)	Pearlite (%)	AF or B (%)
F-P	A1	9.6	90.7	9.3	-
	A2	20.4	91.2	8.8	-
	A3	11.8	93.0	5.2	1.8
	B	6.8	98.3	1.7	-
F-AF	A4	7.4	80.5	8.1	11.4
	A5	7.2	75.9	-	24.1
	C	4.3	88.7	1.7	9.6
AF-F	D	4.6	5.9	2.1	92
	E	4.2	5.5	1.1	93.4
	F	-	-	2.2	97.8
B	G1	-	3.0	-	97.0
	G2	-	2.1	-	97.9
	G3	-	1.8	-	98.2

Where, F- Ferrite, AF- Acicular Ferrite, P- Pearlite, B- Bainite

An investigation of the tensile properties shows that, steels with the bainite structure have the highest strength followed by the acicular ferrite–ferrite steels, then ferrite–acicular ferrite steels and then

Table 2:

ferrite–pearlite steels. The following table lists the tensile and impact properties of the various steels, along with the figure illustrating a correlation between Yield strength and Yield ratio.

Steel	YS (MPa)	UTS (MPa)	EL (%)	YR (%)	DBTT (°C)	Upper Shelf Energy (J)
A1	465	555	42.5	83.8	-51	406
A2	458	553	40.5	82.9	-15	400
A3	456	550	37.2	82.9	-31	400
B	469	523	31.2	89.5	-82	421
A4	489	583	35.0	83.9	-40	371
A5	508	582	36.5	87.3	-25	349
C	543	618	25.4	87.9	-79	305
D	587	707	23.7	83.0	-78	266
E	592	719	24.2	82.5	-90	212
F	588	697	19.2	84.4	-63	179
G1	575	718	15.3	80.2	-28	272
G2	629	747	14.7	84.2	-12	255
G3	653	757	11.8	86.2	3	258

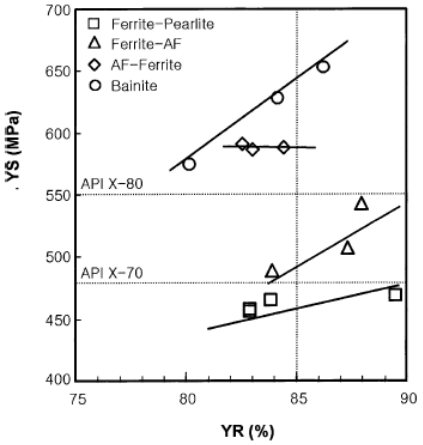

Fig: Relationship of Yield Strength to Yield ratio [4]

This data sheet could be used to study and model a correlation between the different microstructural constituents such as grain size and volume percentage to the mechanical properties. One expression that has been pointed out to describe the relationship between the yield ratio and work hardening exponent as per the Swift equation is as follows:

$$YR = \frac{S_y}{S_u} = \frac{(b + \ln(1+e_y))^N}{(1+e_y)} \frac{\exp(N-b)}{N^N} \quad \text{....Eq(1)}$$

Where YR is the yield ratio, S_y is the yield strength, S_u dditive strain constant, e_y is the engineering strain at yield strength (usually 0.002), and N is the work hardening exponent [4].

Table 3:

Structure	b	N*
Ferrite-Pearlite	0.03	0.1738
Ferrite-Acicular Ferrite	0.03	0.1738
Acicula Ferrite-Ferrite	0.01	0.1175
Bainite	0.002	0.0796

Values of b and N to achieve the yield ratio of 0.85 [4]

3. Strength correlation to the different phases of steel

The APIL X42 grade of steel belongs to the category of HSLA steel is known to be composed of a ferrite-pearlite microstructure, with strengthening micro constituents as Nb and Vn. Hence, the impact of Ferrite, pearlite, and ferrite-pearlite microstructure will be discussed in this section, however, the impact of the other phases on strength can also be obtained from the reference literature.

Ferrite

This phase consists of solid solution of Iron, carbon and other alloying elements and essentially dissolves very low carbon with room temperature solubility being less than 0.005%. As per this reference literature, the strength of a pure ferritic steel can be determined by its grain size according to the Hall-Petch relationship:

$$\sigma_Y = \sigma_o + k_y d^{-1/2}$$

Where, σ_o and σ_Y are constants and d is the ferrite grain diameter as can be o ....Eq(2)m a representative microstructure of Fig. below:

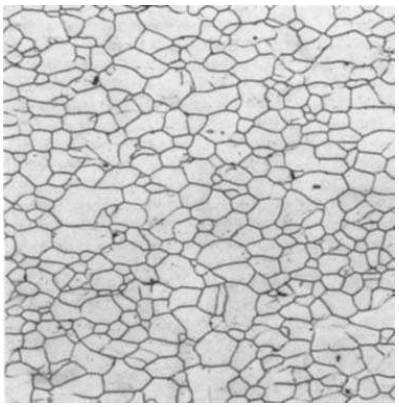

Fig: Microstructure of a fully ferritic, ultralow carbon steel. Marshalls etch + HF, 300x. Courtesy of A.O. Benscoter, Lehigh University [5]

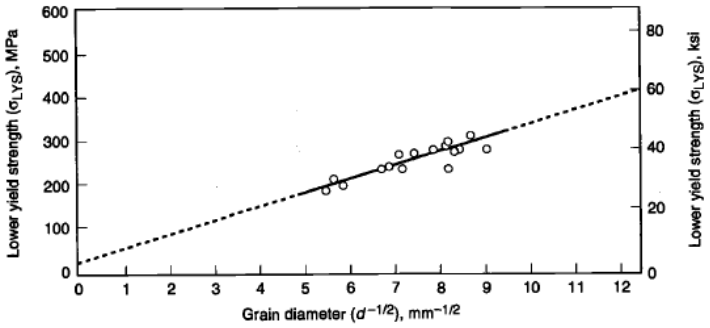

Fig: Hall-Petch relationship in low C ferritic steels [5]

This phase consists of a composite microstructure with parallel plates or lamellaes of a very hard carbide phase, cementite, and a very soft and ductile ferrite phase. A fully pearlitic microstructure is observed at the eutectoid composition of 0.78% C. The yield strength relationship as per Heller can be described as:

$$\sigma_y = -85.9 + 8.3(\lambda^{-1/2}) \quad \text{....Eq(3}$$

Where, is the 0.2% offset yield strength and and X is the interlamellar spacing (in mm).

It has also been shown by Hyzak and Bernstein that strength is related to interlamellar spacing, pearlite colony size, and prior-austenite grain size, according to t h e following relationship:

$$YS = 52.3 + 2.18(\lambda^{-1/2}) - 0.4(d_c^{-1/2}) - 2.88(d^{-1/2})$$

where YS is the yield strength (in MPa), d e is the pearlite colony size (in mm), a ....Eq(4 prior austenite grain size (in mm).

Both these equations show that composition doesn't have a major role to play in the yield strength of fully pearlitic eutetctoid steel and is rather controlled by interlamellar spacing, colony size, and prior-austenite grain size.

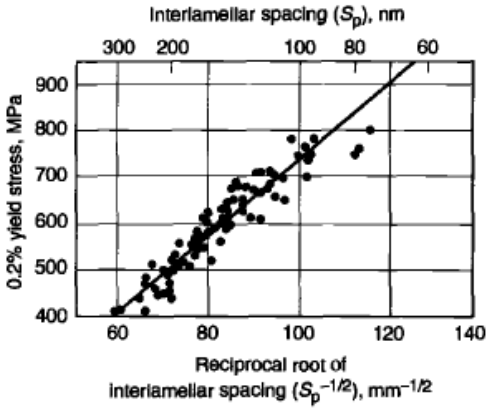

Fig: Relationship between pearlite interlamellar spacing and yield strength for eutectoid steels [5]

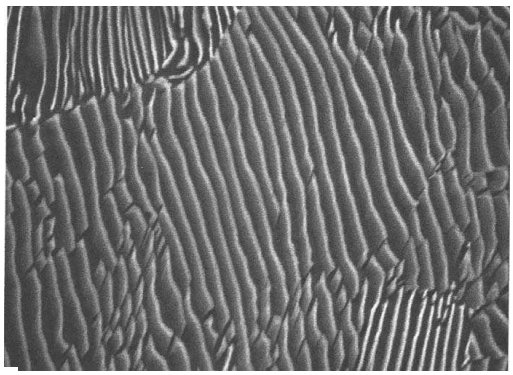

Fig: SEM micrograph of a pearlite phase [5]

Interlamellar spacing can be determined with the use of a scanning electron microscope (SEM), or a transmission electron microscope (TEM), with a resolution of with a 10KX magnification.

It is very difficult to measure the colony size and especially the prior-austenite grain size and require a skilled metallographer using the light microscope or SEM and special etching procedures.

Ferrite-Pearlite

The properties of these types of steels are governed by carbon content and the grain size. The UTS is known to increase with the C content mostly due to the increase in the volume fraction of pearlite in the microstructure. However, as the yield strength is controlled by the ferrite matrix, it remains relatively unaffected by the C content.
One of the empirical relations for strength and microstructural features correlation for ferrite-pearlitc steels under 0.25% C is as follows:

$$YS = 53.9 + 32.34\,(\mathrm{Mn}) + 83.2(\mathrm{Si}) + 354.2(N_f) + 17.4(d^{-1/2}) \quad \text{....Eq(5)}$$

Where, where Mn is the manganese content (%), Si is the silicon content (%), Nf is the free nitrogen content (%), and d is the ferrite grain size (in mm) [5]

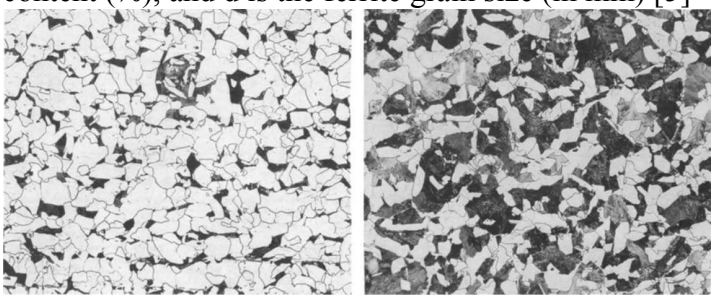

Fig: Microstructure of typical ferrite-pearlite structural steels at two different carbon contents. (a) 0.10% C. (b) 0.25% C. 2% nital + 4% picral etch. 200x [5]

4. Strength correlation to hardness of steel

A general well known relationship between hardness and strength for the non-work hardening behavior established by Ashby and Jones and Tabor follows:

$$H_V \approx 3 \cdot \sigma_y. \quad \text{....Eq(6)}$$

Where, Hv is the Vickers Hardness and yield strength.

Some other literature attempt to further study the correlation of the yield strength and the tensile strength to the diamond pyramid hardness values for these steels, with the use of regression analysis. Both of these exhibit a linear relationship to hardness. Also, an effect of strain hardening potential on a hardness-yield strength relationship has been illustrated.
As described by Cahoon et al. [Ref 8,9] hardness and tensile strength and yield strength can be related as follows:

$$\mathrm{TS} = \left(\frac{H}{2.9}\right)\left(\frac{n}{0.217}\right)^n$$

$$\mathrm{YS} = \left(\frac{H}{3}\right)(0.1)^n \quad \text{....Eq(7)}$$

where H is the hardness in kg_f/mm^2 TS and YS are tensile strength and yield strength, respectively, and n is the strain-hardening exponent. These expressions are usually good for tensile properties of a ferritic steel upto 400 deg C.

Further equations have been developed to estimate these strengths based off of bulk hardness measurement. One such experiment gives in a result as:

YS= -90.7 + 2:876 Hv,
TS= -99:8 + 3.734 Hv ....Eq(8)

Where yield and tensile strength have units of MPa and Hv is the Vickers Hardness in (kg_f/mm^2)

Another study involved development of a statistical correlation of strength-hardness relationship of API X 65 steel grades which predicted the following relationships; [6]

YS=2×HV+105, R^2 = 0.2 ….Eq(9)
UTS=1.3×HV+344, R^2 = 0.8

5. Hardness Correlation to CEV

The concept of Carbon equivalent was first developed by Dearden and O'Neil [10], and the final form of the modified equation is:

CE= C + (Mn + Cr)/5.5 + Ni/15 + V/5 + Mo/4 + Co/150 + P/2 ….Eq(10)

This equation can be used with the following equation to predict the hardness of steel and hence correlate it to the strength.

Hv = 120CE – 200 ….Eq(11)

The composition of the different elements can be determined with the use of EDS or OES depending on the scale of the testing required [7].

SECTION III:

References:

1. Swastik Pipes Limited(2008). *Mechanical and Chemical Properties of API 5L*. Retrieved from http://www.swastikpipes.com/api_pipes.html
2. Advanced Technology Corporation (September 1999). *Nondestructive Determination of Yield Strength and Stress-Strain Curvesof In-Service Transmission Pipelines Using Innovative Stress-Strain Microprobe Technolog.* Retrieved from http://www.atc-ssm.com/pdf/dotpipe-fr.pdf
3. Thomas Hoper.Shigeru Endo.Nobuyuki Ihikawa and Koichi Osawa (1999). Effect of Volume Fraction of Constituent phases on the stress-strain relationship of Dual Phase Steels. *ISIJ International, Vol. 39.*
4. Y. M. KIM, S. K. KIM,1) Y. J. LIM2) and N. J. KIM (2002). Effect of Microstructure on the Yield Ratio and Low Temperature Toughness of Linepipe Steels. *ISIJ International, Vol. 42.*
5. Bruce L. Bramfitt (1998). Structure/Property Relationships in Irons and Steel, *Bethlehem Steel Corporation. ASM International.*
6. Chester Vantyne (November 2008). Correlation of Yield Strength and Tensile Strength with Hardness for Steels. *Journal of Materials Engineering And Performance.*
7. Wesley Wang. The Great Minds of Carbon Equivalent. Retrieved from https://ewi.org/eto/wp-content/uploads/2015/10/Great-Minds-of-Carbon-Equivalent-Pt1-Wang-FINAL.pdf
8. J.R. Cahoon, W.H. Broughton, and A.R. Kutzak, The Determination of Yield Strength from Hardness Measurements, Metall. Trans.,1971, 2, p 1979–1983
9. J.R. Cahoon, An Improved Equation Relating Hardness to Ultimate Strength, Metall. Trans., 1972, 3, p 3040.
10. Dearden, J. and O'Neill, H., "A Guide to the Selection and Welding of Low Alloy Structural Steels", *Transactions of the Institute of Welding*, Vol III, pp. 203-214, 1940

SECTION IV:

1. Introduction:

The United States transports liquid petroleum over 190,000 miles whereas the natural gas pipeline system is a massive underground network of over 2.4 million miles [1]. About 67% of the total crude oil pipelines were laid down before 1980 [2]. Hence, on an average, the age of the pipes currently in use is approximately 35 years in service. Over a period of time, due to the internal as well as external conditions of the pipelines, they deteriorate gradually. Corrosion is the main cause for deterioration of the pipelines. The integrity of the pipeline is important to avoid leakage, leading to safety and environmental hazards and tremendous losses. Of the hazardous liquid pipeline accidents caused by corrosion, 65% were due to external corrosion and 34% were due to internal corrosion. For, natural gas transmission pipeline accidents, 36% were caused by external corrosion and 63% were caused by internal corrosion [3]. Thus, testing of pipelines for its material properties and strength has become of prime importance. Conventional mechanical tests require a large amount of test material and in most of the cases this may not be available from the components that are in service. Therefore, it is of great importance to develop methods which can be performed in-situ. Since the testing is carried out in-situ, it needs to be non-destructive or minimally destructive in order to serve the purpose of testing [4]. The automated ball indentation (ABI) test is based on strain-controlled multiple indentations (at the same penetration location) of a polished surface by a spherical indenter (0.25 to 1.57-mm diameter). The microprobe system and test methods are based on well demonstrated and accepted physical and mathematical relationships which govern metal behaviour under multiaxial indentation loading [5].

The objective of the research project is to determine the mechanical properties (toughness, yield strength, ultimate tensile strength etc.) of a material specimen using ABI testing. An electromechanical MTS testing machine, capable of a maximum loading of 10kN is being used to carry out the ABI testing. To fit the indenter in the machine, a fixture has been designed for the top head of the machine. Another fixture has been designed for the bottom head to hold the testing specimen in place. The displacement and load of the indenter can be monitored on a computer connected to the machine. Simulation for the loading of the indenter on a steel test specimen is being carried out using ABAQUS. Results from both, the testing and simulation will be compared in order to gauge the error in the testing and validate the results.

2. Design of Top Head fixture:

The MTS machine has a load cell which has a threaded connection extending downwards. A hollow shaft of about 50mm in length with an extension as shown in figure 1 has been designed and manufactured for the top head of the MTS machine. A ball indenter of diameter 1.58mm fits into the slot of the fixture. The indenter is held in place with the help of a bolt as shown in the figure below.

Fig. 1 Top head fixture on the MTS machine

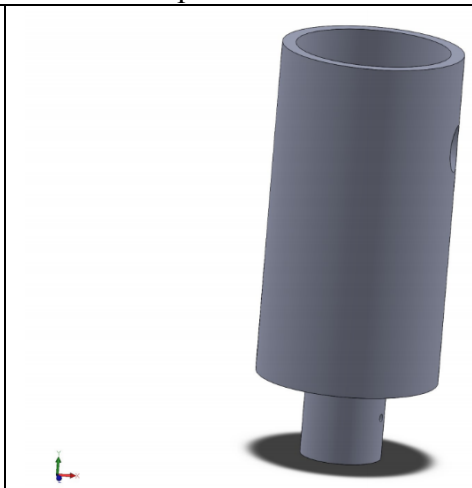

Fig. 2 Model of the top head fixture

3. Design of Bottom Head Fixture:

The bottom head of the MTS machine has an existing arrangement of a hollow shaft centred on a hexagonal nut on the base of the MTS machine. A fitting shaft has been manufactured for the slot in the bottom head of the MTS machine. The top face of the fixture will be used to mount the specimen. The arrangement is made such that the shaft fits tightly in the slot of the bottom head. It is ensured that no movement of the flat base of the bottom fixture is possible. The top surface is made as smooth as possible. A 3D model in SolidWorks of the fixture for the top and bottom head is shown in figures 2 and 4 respectively.

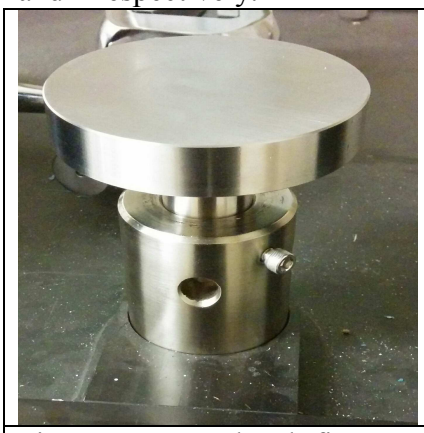

Fig. 3 Bottom head fixture on the MTS machine

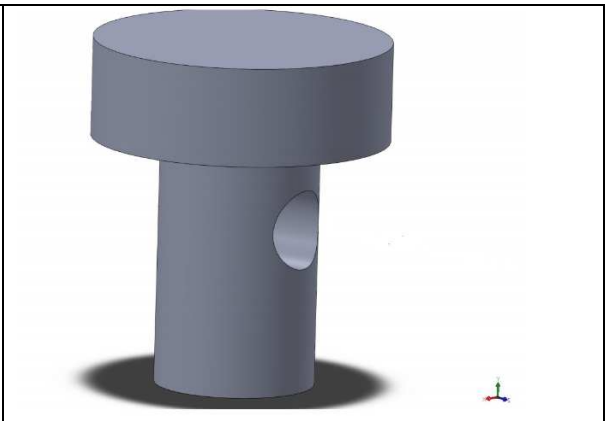

Fig. 4 Model of bottom head fixture

4. Modelling:

The geometry of the indenter and plate is modelled in ABAQUS as shown in figure 5, where the indenter is considered to be a rigid body, given its high hardness and the plate material is considered to be steel with elastic-plastic deformation occurring due to the contact. The material properties used for the steel plate are summarized as given below:

Modulus of Elasticity – 210.7GPa

Poisson's Ratio – 0.303

Yield stress (MPa)	Plastic Strain
200.2	0
246	0.02353
294	0.0474
374	0.09354
437	0.1377
480	0.18

Table 1. Plastic properties for steel

Boundary conditions are applied on the plate and indenter so as to simulate the contact of the pair. The bottom face of the plate was fixed and the load is applied on the top face of the indenter. The boundary conditions applied are shown in figure 6. While defining the contact pair, the plate is made the master surface whereas the indenter is considered as the slave surface.

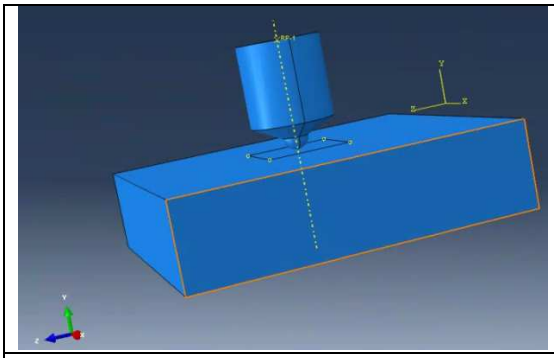

Fig. 5 Indenter-plate assembly model

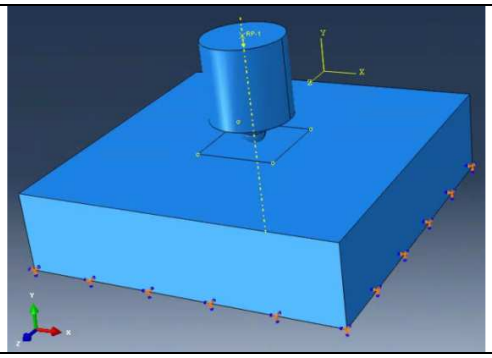

Fig. 6 BC and loading of assembly

The model was meshed using various control parameters such as edge divisions to achieve good quality elements in the desired region. Tet elements were used for the indenter as its body had a curved surface. After meshing, material model was assigned for each of the bodies.

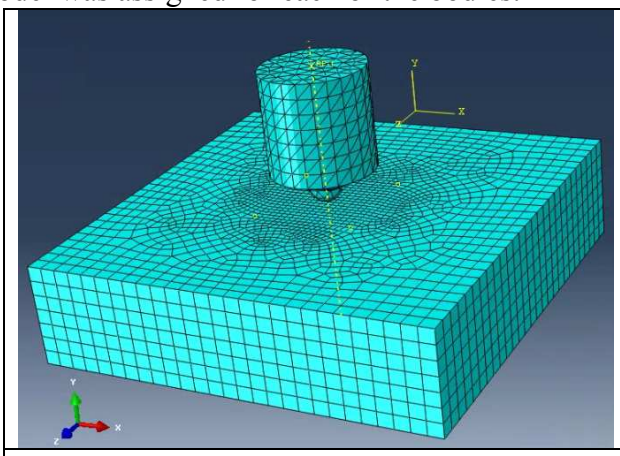

Fig. 7 Meshed model of assembly

References:

[1] American Petroleum Institute: http://www.americanpetroleuminstitute.com/Oil-and-Natural-Gas-Overview/Transporting-Oil-and-Natural-Gas/Pipeline

[2] Inside Energy: http://insideenergy.org/2014/08/01/half-century-old-pipelines-carry-oil-and-gas-load/

[3] ASME: http://www.asminternational.org/documents/10192/1849770/ACFAB96.pdf

[4] Das, M., Pal, T. K., and Das, G., 2012, "Use of Portable Automated Ball Indentation System to Evaluate Mechanical Properties of Steel Pipes," Trans. Indian Inst. Met., **65**(2), pp. 197–203.

[5] Haggag, F. M., 1993, "In-situ measurements of mechanical properties using novel automated ball indentation system," ASTM Spec. Tech. Publ., pp. 27–44.

Task 2. Experimental testing, data analysis and prototyping for acoustic and micro-electromagnetic electromagnetic properties of pipe steel

In the 1st quarter, CU team leveraged the research findings in CAAP14 and continued to develop the micro-electromagnetic sensing prototype as proposed in the project. The sensor development effort was assisted by the 3D numerical simulation as well as the fast imaging research using innovative continuous data acquisition, which will be summarized in this section.

Task 2.1 – Multi-channel sensor prototyping

In this quarter, we designed and fabricated the multi-channel scanning sensor tip the control circuit for the multi-channel scanning sensor for improving the scanning speed. A control circuit also has been designed same setup as the current experiment. The innovative design of the control circuit shows in Fig. 1(a). Compared with the current experiment, shown in Fig. 1(b), the control circuit compresses the directional coupler, RF to AC converter and data collection together to perform the same function. The control circuit uses a microcontroller to control the input and receive signal. There is no connection between data processing and receiving signal in the control circuit design, which will reduce the scanning time.

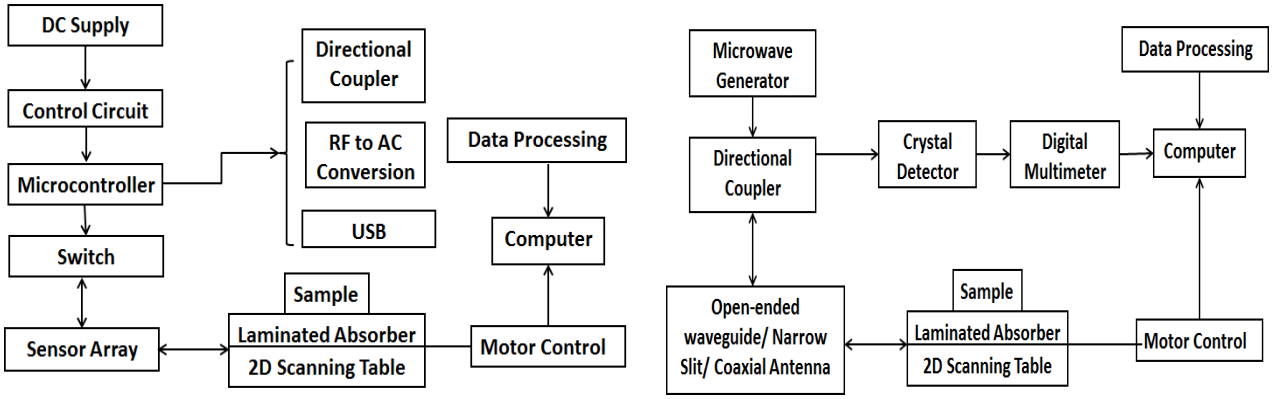

(a) Improved design with Control circuit (b) Current experiment design

Fig. 1 Design comparison of control circuit and current experiment setup

The control circuit schematic is shown in Fig. 2. We had several difficulties while designing the control circuit. First is how to split the signal equally to each channel. This is important to the experiment to make sure the signal level is equal. We planned to use PCB trace to build the splitter. Since the operation frequency of the scanning sensor is at 3GHz, it is difficult to avoid the noise if we have long traces on PCB. Instead of building a splitter, we chose to use a high speed switch to control the signal. The switch will allow the signal transfer to each probe sequentially. This will avoid the noise generated between the traces, also help avoid the noise that generate between the probes. The second problem we encountered during the design was how to store the return signal data. The goal of the design is for the field testing in the future. How to effectively store the data is important. Instead of using NI DAQ card as we do in our experiment, we chose to use a USB port for storing data for later processing. This will allow the design to be portable for future field testing. The USB port will also help reduce the scanning time since there is no data processing involved. The last question we had during the design process is how to generate the maximized input the signal. Even though the scanning sensors are designed for 3GHz signal, there will be slightly difference between each probe due to the machine error. To be able to adjust the frequency to maximize the signal would be another requirement for the control circuit. We chose Voltage Control Oscillator (VCO) to control the input signal. This will give us the freedom to adjust the input signal to obtain the better resolution.

The fabricated control circuit board and array antenna show in Fig. 3. The size of the circuit is approximately 8cm by 8cm. The next step is to program the IC to control the high speed switch for each element of array to radiate and receive signal. The design of the control circuit also has the ability for future expansion to up to 8 channels.

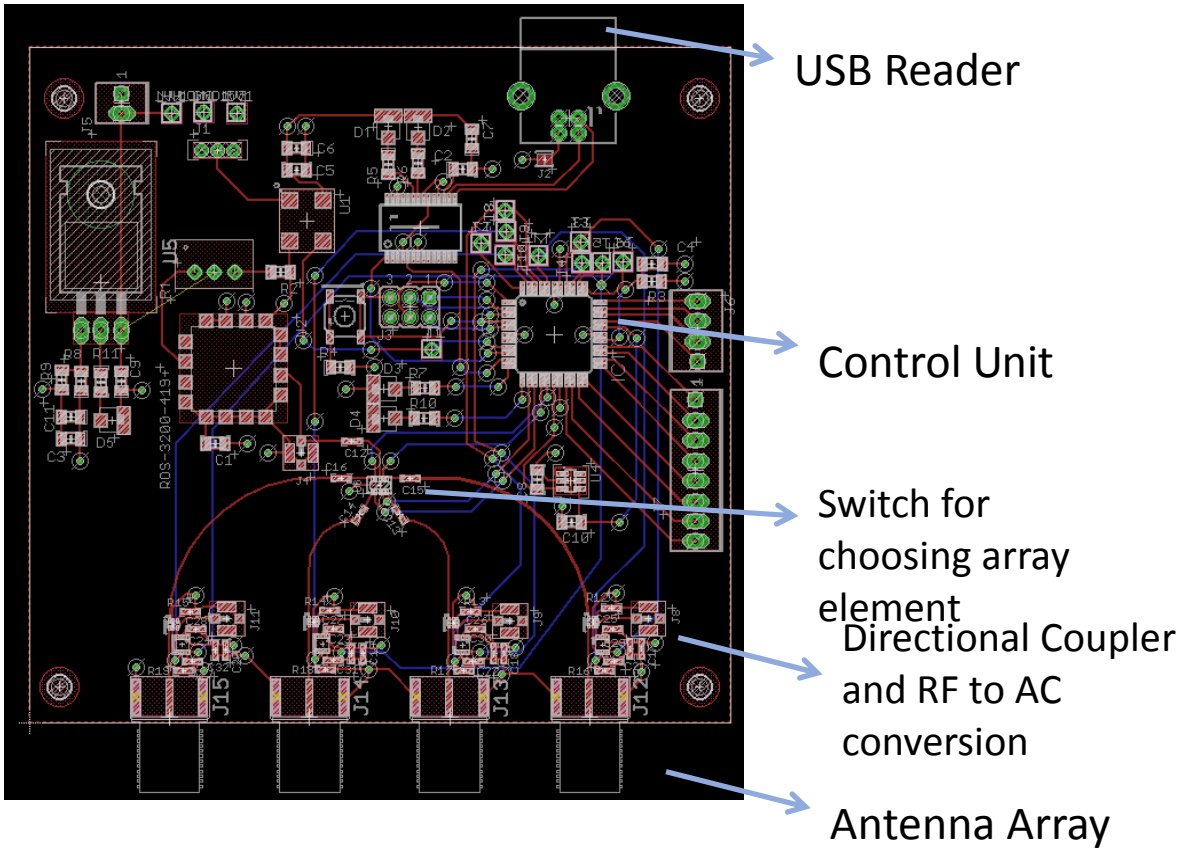

Fig. 2 Control Circuit Design

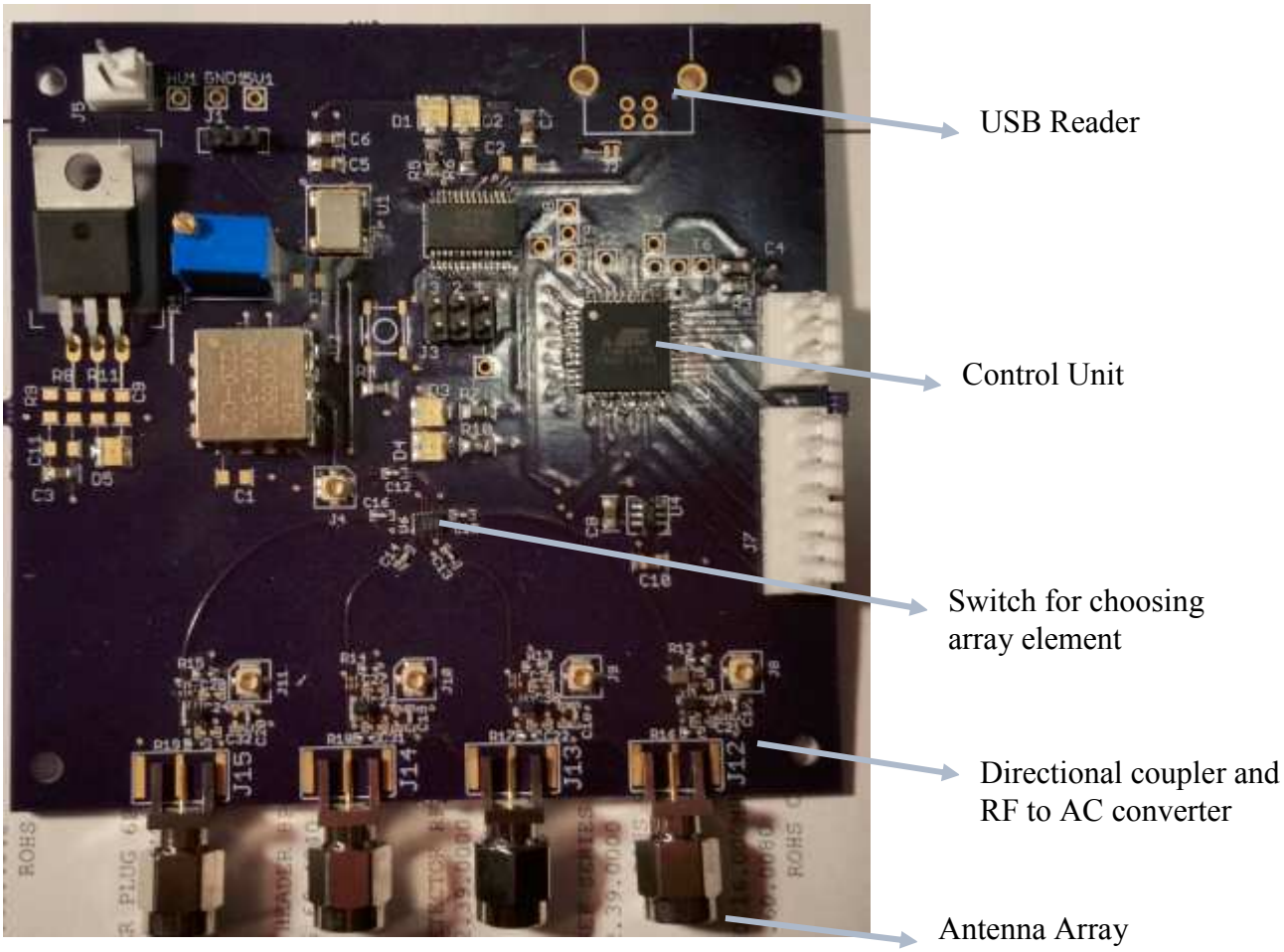

Fig. 3 Control Circuit and Antennas for multi-channel sensor design.

Task 2.2 – 3D Model of Near-field Microwave Sensing

For ideal lossless dielectric with excitation J, Maxwell equation can be written as:

$$-\nabla \times E = j\omega\mu H \quad (1)$$
$$\nabla \times H = j\omega\epsilon + J \quad (2)$$
$$\nabla \cdot E = \frac{1}{\epsilon}\rho \quad (3)$$
$$\nabla \cdot H = 0 \quad (4)$$

The electric field and Magnetic Field introduce by excitation J can be described by

$$E = -j\omega\mu A - \nabla\varphi \quad (5)$$
$$H = \nabla \times A \quad (6)$$

According to Lorentz gauge, the relationship between magnetic vector potential A and electric scalar potential ϕ is:

$$\nabla \cdot \mathrm{A} = -\mathrm{j}\omega\varepsilon\varphi \qquad (7)$$

Substitute (5),(6),(7) into (1),(2):

$$\nabla^2 A + k^2 A = -J \qquad (8)$$

$$\nabla^2 \varphi + k^2 \varphi = \frac{1}{j\omega\varepsilon} \nabla \cdot J \qquad (9)$$

For lossless media, $\mathrm{k} = \omega\sqrt{\mu\varepsilon}$

The solution of vector and scalar Helmholtz equation in the infinite space can be expressed as:

$$\mathrm{A(r)} = \int_v J(r')G(R)dv' \qquad (10)$$

$$\varphi = \frac{-1}{j\omega\epsilon} \int_v \nabla' \cdot \mathrm{J}(r')\mathrm{G(R)}\, dv' \qquad (11)$$

$\mathrm{G(R)}$ is the green function in the infinite space. R is the distance between observation point and the middle of the antenna. $\mathrm{G(R)} = \frac{e^{-jkR}}{4\pi R}$

The Integral form of the EM field can be described by substituting (10),(11) into (5) ,(6) and do vector transformation:

$$\mathrm{E(r)} = -\mathrm{jkZ} \int_v [J(r')G(R) + \frac{1}{k^2} \nabla' . J(r') \nabla G(R)] dv' \qquad (12)$$

$$\mathrm{H(r)} = -\int_v J(r') \times \nabla G(R) dv' \qquad (13)$$

By applying equivalence principle algorithm, we can get the electric field integral equation of the surface of nylon plate. Equivalence principle algorithm (EPA) was first proposed by Chew in 2006. It based on the Huygens' Principle and exploits cubical surfaces to support equivalent sources. Consider an area with boundary, if the distribution of the source inside of the area is unchanged and outside of the area distribute different source. If the fields generated by those source satisfy the same boundary condition then the uniqueness theorem guarantees that there is only one solution to the problem which means we can find the relationship between source and field from the other pair. For some cases it will bring great convenience to the solve problem with the equivalent source instead of the actual source.

If the V_1 (ε_0, μ_0) is the free space and V_2 (ε_1, μ_0) is a polyamide plate. S is the surface of the polyamide plate and n_1, n_2 are the exterior normal and inner normal.

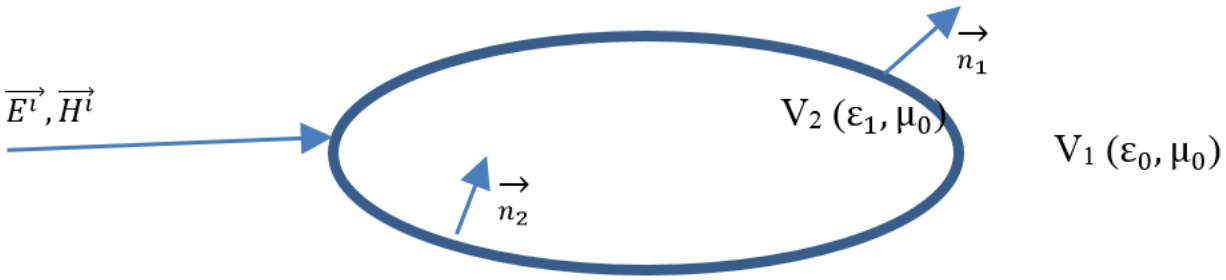

Fig. 4. Equivalence principle Schematic

V_2 is passive. Surface current and surface magnetic current of S is:

$$\overrightarrow{J_s} = \overrightarrow{n_1} \times \overrightarrow{H_1}\ , \quad \overrightarrow{M_s} = -\overrightarrow{n_1} \times \overrightarrow{E_1} \qquad (14)$$

$\overrightarrow{E_1}, \overrightarrow{H_1}$ is the electric field and magnetic field on the S. According to uniqueness theorem, $\overrightarrow{J_s}$ and $\overrightarrow{M_s}$ are the equivalence source of V_2. Set an antenna locate in V_1 perpendicular to v_2. Under the excitation of $\overrightarrow{E^i}$, $\overrightarrow{E_1}$ and $\overrightarrow{H_1}$ on the S can be described as:

$$\overrightarrow{E_1} = \overrightarrow{E^i} + \overrightarrow{E^s}\ , \ \overrightarrow{H_1} = \overrightarrow{H^i} + \overrightarrow{H^s} \qquad (15)$$

Therefore $\overrightarrow{J_s}$ and $\overrightarrow{M_s}$ can be written as:

$$\overrightarrow{n_1} \times \overrightarrow{E_1}(\vec{r}) = \overrightarrow{n_1} \times \overrightarrow{E^i}(\vec{r}) + \overrightarrow{n_1} \times \oint [-j\omega u_0 g_0 \overrightarrow{J_s} - \frac{j}{\omega \varepsilon_0} \nabla \cdot \overrightarrow{J_s} \nabla g_0] ds \quad (16)$$

$$\overrightarrow{n_2} \times \overrightarrow{E_2}(\vec{r}) = \overrightarrow{n_2} \times \oint [-j\omega u_0 g_0 \overrightarrow{J_s}' - \frac{j}{\omega u_1} \nabla \cdot \overrightarrow{J_s}' \nabla g_2 + \overrightarrow{M_s}' \times \nabla g_2] ds \quad (17)$$

$$\overrightarrow{n_1} \times \overrightarrow{E_1}(\vec{r}) = \overrightarrow{n_1} \times \overrightarrow{E^i}(\vec{r}) + \overrightarrow{n_1} \times \oint [-j\omega u_0 g_0 \overrightarrow{J_s} - \frac{j}{\omega \varepsilon_0} \nabla \cdot \overrightarrow{J_s} \nabla g_0] ds \quad (16)$$

$$\overrightarrow{n_2} \times \overrightarrow{E_2}(\vec{r}) = \overrightarrow{n_2} \times \oint [-j\omega u_0 g_0 \overrightarrow{J_s}' - \frac{j}{\omega u_1} \nabla \cdot \overrightarrow{J_s}' \nabla g_2 + \overrightarrow{M_s}' \times \nabla g_2] ds \quad (17)$$

$$g_i = \frac{e^{jk_i|\vec{r}-\vec{r}'|}}{4\pi|\vec{r}-\vec{r}'|} \quad , k_i = \omega\sqrt{\mu\varepsilon_i} \ (i = 0,1) \quad (18)$$

Since the tangential component of E is continuous across the interface,

$$\overrightarrow{n_1} \times \left(\overrightarrow{E_1} - \overrightarrow{E_2}\right) = 0 \,, \quad \overrightarrow{n_1} \times \left(\overrightarrow{H_1} - \overrightarrow{H_2}\right) = 0 \ (19)$$

Consider (19), and:

$$\overrightarrow{n_1} = -\overrightarrow{n_2} \,, \overrightarrow{J_s}' = -\overrightarrow{J_s} \,, \overrightarrow{M_s}' = -\overrightarrow{M_s} \quad (20)$$

The sum of (17) and (18) is

$$\overrightarrow{n_1} \times \overrightarrow{E^i}(\vec{r}) = \overrightarrow{n_1} \times \oint [-j\omega u_0 \overrightarrow{J_s}(g_0 + g_1) + \frac{j}{\omega \varepsilon_0} \nabla \cdot \overrightarrow{J_s} \nabla (g_0 + \frac{\varepsilon_0}{\varepsilon_1} g_1) - \overrightarrow{M_s} \times \nabla (g_0 + g_1)] ds \quad (21)$$

$$\overrightarrow{n_1} \times \overrightarrow{H^i}(\vec{r}) = \overrightarrow{n_1} \times \oint [j\omega u \varepsilon_0 \overrightarrow{M_s}(g_0 + \frac{\varepsilon_1}{\varepsilon_0} g_1) + \frac{j}{\omega \mu_0} \nabla \cdot \overrightarrow{M_s} \nabla (g_0 + g_1) + \overrightarrow{J_s} \times \nabla (g_0 + g_1)] ds \quad (22)$$

For far field, $\overrightarrow{E^i}$ can be considered as a plane wave and the value will be constant. For near field, $\overrightarrow{E^i}$ is a spherical wave

$$\overrightarrow{E^i}(\vec{r}) = E_0^i r_0 \frac{e^{jk|\vec{r}'-\vec{r}_T|}}{|\vec{r}'-\vec{r}_T|} e^i_{(\vec{r}')} \quad (23)$$

Since $\overrightarrow{E^i}(\vec{r})$ is a function of distance, the value of $\overrightarrow{E^i}(\vec{r})$ is different at different location. Therefore, $\vec{r}_T$ has to be taken into consideration. From above equations, we can calculate the distribution of current and magnetic current on the surface *S* and then we can get the equation of scattered field:

$$\overrightarrow{E^s} = \oint [-j\omega u_0 g_0 \overrightarrow{J_s} - \frac{j}{\omega \varepsilon_0} \nabla \cdot \overrightarrow{J_s} \nabla g_0 + \overrightarrow{M_s} \times \nabla g_0] ds \quad (24)$$

Since equation (21), (22) are too complex to solve by analytic method. Therefore we apply numerical method to get an approximate solution. Set nodes r_i (i=1~N) on the surface of V_2.

$$u^h(\mathrm{r}, \vec{r}) = \sum_i^m P_i(r) a_i(\vec{r}) = P(r) a(\vec{r}) \quad (25)$$

For each nodes assign influence of domain d_i and introduce weight function $W_i(r - r_i)$.

$$u^h(\mathrm{r}, \vec{r}) = P \ \ (r)[P^T w(r) P]^{-1} P^T w(r) = \sum_{i=1}^n \varphi_i(r) u_i \quad (26)$$

Task 2.3 Fast imaging acquisition for sensor optimization

Near-field microwave microscopic (NFMM) imaging method is a very useful sensing technique which based on the contrast in electromagnetic properties of the media. It able to providing desirable diagnostic capabilities for applications in several areas. However, Speed is an issue of current single sensor imaging. The initial scanning time for a small area is still very long. A scan of 190 mm x 100 mm area with step size 0.635 mm will cover 48,000 spatial locations. The scanning system applies step by step scanning method will stop at each spatial location and calculate spatial value by averaging 3000 samples. Therefore, to complete an entire scan the system will stop 48,000 times and process 144 million samples during the scanning. It will result in a very long operating time. Another disadvantage of step by step scanning system is the strong. Step by step scanning system repeats moving and stop at each spatial location and introduce vibration and result in inaccuracy.

For a better scan speed and performance, a continuous scanning method which avoid disadvantages mentioned above is under development. In the continuous scanning system, motor will continuous moving until reach the end of each column instead of stop at each spatial location.

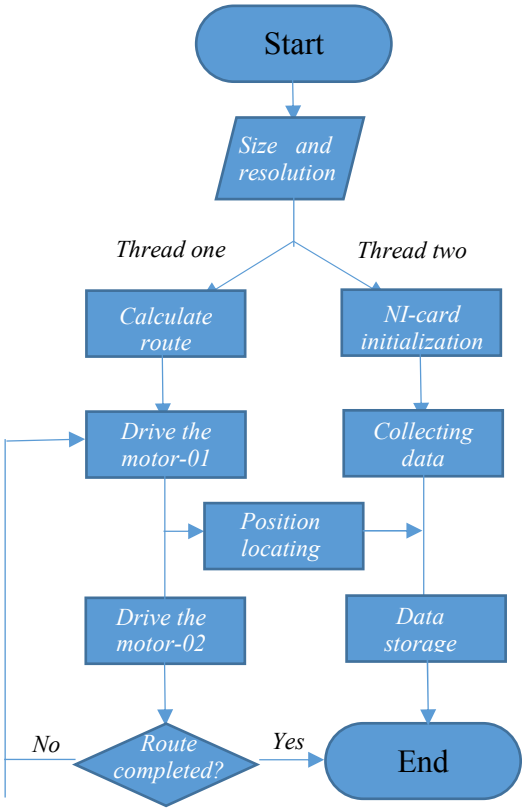

Fig.5. Flow chart of the two thread.

As Fig. 5 shown above, a python code which controls two step motors and collects data at same time has been programmed. This code contains two threads. Thread one calculates the route of the motors according to the size of the scanning sample and drives the motors. Thread two collects the data read from NI-DAQ card and records the position current scanning.

After inputting the length and width of the sample and deciding the resolution of the scan, the thread one will calculate the route of the entire scan. The route will cover the sample and the distance between each line is decided by the resolution. In the meantime, thread two will initialize the NI-card such as the communications protocols and sampling rate. Higher sampling rate will give a better result but also require more computational capabilities. When calculation of the route is completed, thread one will drive the motor01 to move the sample and read the feedback from motor01 to determine the position. Thread two keeps collecting the sampling data. Non-stop scanning increase the difficulty of locating point. Therefore, a global variable has been set as the bridge of the two threads to improve the scanning accuracy. Every time the motor01 return a message of status, thread one will check the motor position according to the route plan. The information of location will transmit to thread two via the global variable. When one line has been scanned, thread one will drive the motor02 in order to scan the next line until the route is completed. Thread two will average the samples and store the data into a matrix. At the end of the scan, the matrix will be plot as an image with ‘hot’ color map and the sampling data before averaging will be saved as raw data.

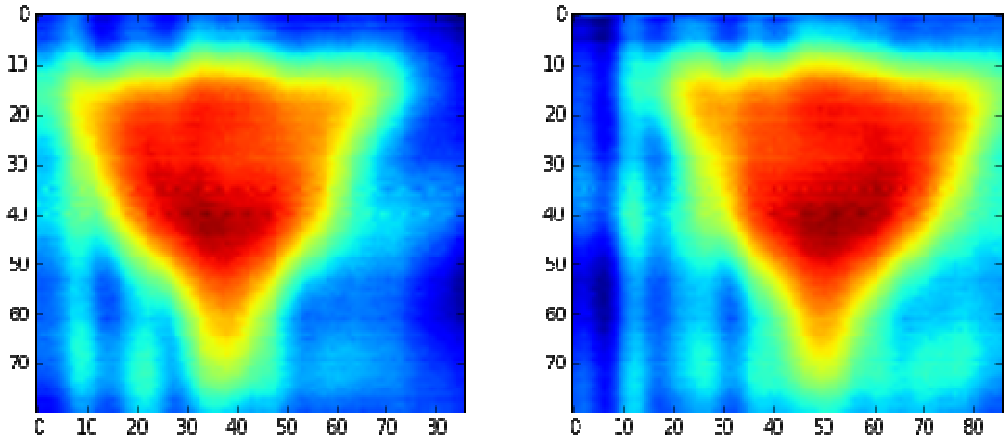

(a) (b)

Fig 6. Continuous scan results of 2x2 inch^2 area: (a) data collected from forward moving and (b) data collected from backward moving.

As Fig. 6 shown above, it is the result image of a 2x2 square inches area with triangle. The sampling frequency is 100 KHz. It takes 0.86 s for the step motor01 moving 2 inches. Therefore, 86000 samples will be acquired for each column. The step size of step motor02 in 200 steps per inches. The size of triangle's raw data is 86000x80 since the setup of this result is acquired data every 5 column. By taking mean of every 1000 data, the size becomes 80x86. It takes about 5 minutes for this entire 2x2 square inches scan.

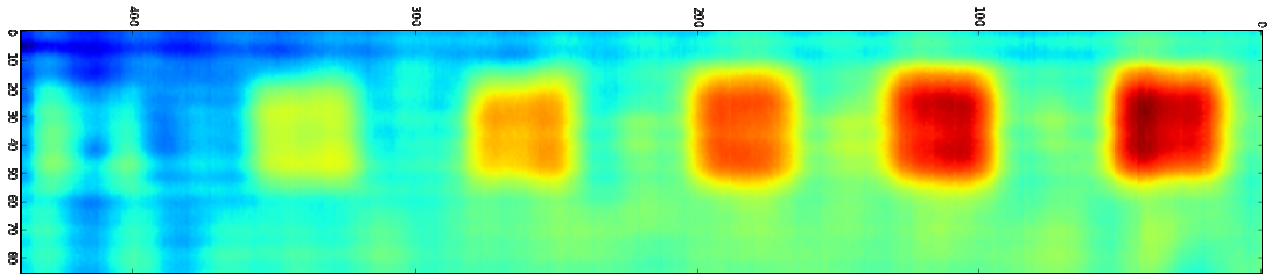

(a). data collected from forward moving

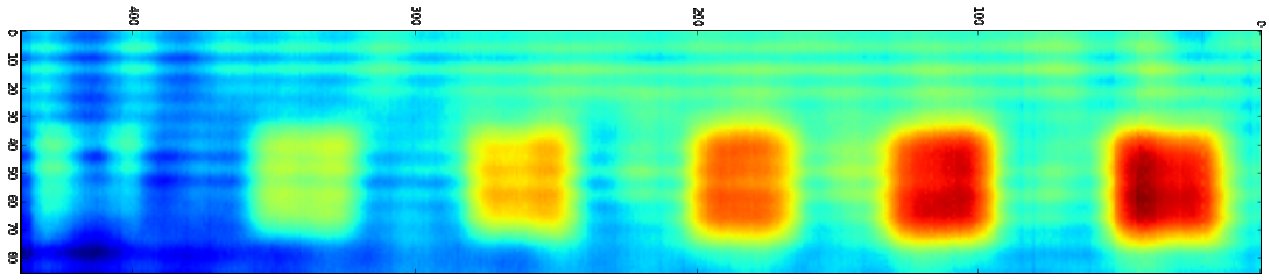

(b). data collected from backward moving

Fig. 7. Continuous scan results of 2x11 inch^2 area

As Fig. 7. shown above, it is the result image of a 2x11 square inches area. The squares shown in the image are with identical size (1x1 inch^2) and different depth. The depth of the squares from left to right are 1mm, 2mm, 3mm, 4mm, 5mm, 6mm. The size of raw data is 86000x440. By taking mean of every 1000 data, the size becomes 86x440. It takes about 20 minutes for this entire 2x11 square inches scan.

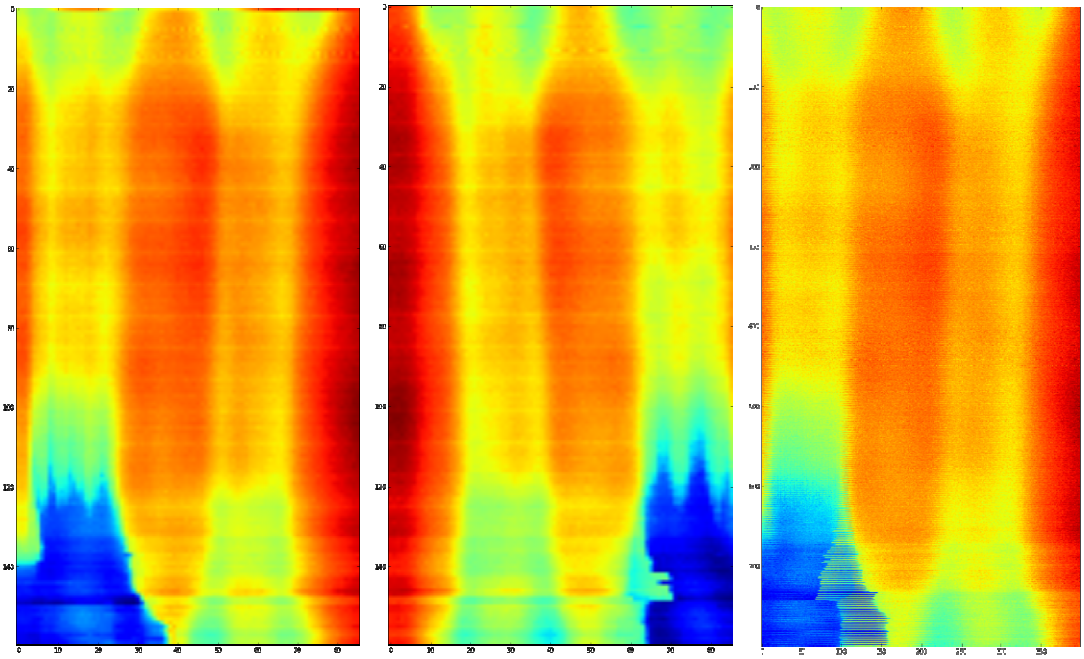

(a). data collected from forward moving (b). data collected from backward moving (c). data collected from step by step

Fig. 8. Continuous scan results and step by step results of 2x8 inch^2 area

The (a) and (b) in Fig. 8 are the result image of continuous scan which took about 7 minutes. Image (c) in Fig. 8. is the result of step by step scan which took more than 2 hours.

References:

[1] Rao, S., D. Wilton, and A. Glisson. "Electromagnetic Scattering by Surfaces of Arbitrary Shape." IEEE Transactions on Antennas and Propagation 30.3 (1982): 409-18. Web.

[2] Jin, Jian-Ming, and Ebooks Corporation. The Finite Element Method in Electromagnetics. Thirdition. ed. Hoboken. New Jersey: John Wiley & Sons Inc, 2014. Web.

[3] Tong, Mei Song, and Weng Cho Chew. "E-Field, H-Field, and Combined-Field Based Nyström Method Analysis for Electromagnetic Scattering by Complex-Material Bodies." IEEE Transactions on Electromagnetic Compatibility 52.3 (2010): 620-8. Web.

[4] Yla-Oijala, P., and M. Taskinen. "Application of Combined Field Integral Equation for Electromagnetic Scattering by Dielectric and Composite Objects." IEEE Transactions on Antennas and Propagation 53.3 (2005): 1168-73. Web.

[5] Peng, Zhen, Kheng-Hwee Lim, and Jin-Fa Lee. "Computations of Electromagnetic Wave Scattering from Penetrable Composite Targets using a Surface Integral Equation Method with Multiple Traces." IEEE Transactions on Antennas and Propagation 61.1 (2013): 256-70. Web.

[6] Volakis, John Leonidas, and Kubilay Sertel. Integral Equation Methods for Electromagnetics. Raleigh, NC: SciTech Pub, 2012. Web.

[7] Parreira, G. F., et al. "The Element-Free Galerkin Method in Three-Dimensional Electromagnetic Problems."IEEE Transactions on Magnetics 42.4 (2006): 711-4. Web.

[8] Liu, Suzhen, et al. "Application of Element Free Galerkin Method to Three Dimensional Electromagnetic Computations".Web.

[9] Chew, Weng Cho. Waves and Fields in Inhomogeneous Media. New York: IEEE Press, 1995. Web.

Description of any Problems/Challenges

The project progress is satisfactory according to the schedule of tasks table. Good communications between the PIs, students and program director is well maintained. No technical challenges were identified in this quarter.

(c) Planned Activities for the Next Quarter

Besides the planned activities mentioned in section (b), here are the future work for the next quarter:

1. To obtain the GTI samples and conduct testing in order to obtain information such as microstructure details with the use of Optical Microscope, Scanning Electron Microscope and EBSD available in the ASU Research Laboratories.
2. To investigate the chemical properties of the samples with the Energy Dispersive Spectroscopy in the ASU Research Center.
3. To study the property variation along the pipe wall thickness with the use of the above techniques and ultrasonic thickness guage.
4. To conduct hardness measurements with the use of Leeb Ball Hardness Tester available in lab facilities.
5. To input the data from the different tests and develop a Bayesian network fusion model to integrate the data and calculate the probabilistic strength and toughness of a component.
6. Simulation of loading-unloading cycles for steel.
7. ABI testing of specimen on electromechanical machine
8. Testing the multi-channel near microwave sensing array on proposed materials
9. Continue to develop the 3D electromagnetic modeling to understand the micro-electromagentic phenomena
10. Keep improving the imaging speed using NFMW microscopy.